Determination of the flow field inside a Sonolator liquid whistle using PIV and CFD

Ryan, David J.; Simmons, Mark J.h.; Baker, Michael R.

DOI:
10.1016/j.ces.2017.01.035

Chemical Engineering Science 163 (2017) 123–136

Contents lists available at ScienceDirect

Chemical Engineering Science

journal homepage: www.elsevier.com/locate/ces

Determination of the flow field inside a Sonolator liquid whistle using PIV and CFD

David J. Ryan [a], Mark J.H. Simmons [a,*], Michael R. Baker [b]

[a] School of Chemical Engineering, University of Birmingham, Edgbaston, Birmingham B15 2TT, UK
[b] Unilever Research & Development, Port Sunlight Laboratory, Quarry Road East, Bebington, Wirral CH63 3JW, UK

HIGHLIGHTS

- Experimental and numerical evaluation of flow in a liquid whistle was made.
- CFD average velocities were in excellent agreement with PIV measurements.
- Turbulent flow parameters from CFD were within estimates from PIV data.
- The presence of the blade was less influential than the size of the orifice.

ARTICLE INFO

Article history:
Received 1 November 2016
Received in revised form 11 January 2017
Accepted 16 January 2017
Available online 18 January 2017

Keywords:
Sonolator
Liquid whistle
Turbulence
Emulsification
Orifice

ABSTRACT

PIV experiments and CFD simulations were carried out on a mimic of a pilot scale Sonolator Model A inline liquid whistle mixer (Sonic Corp. USA) for water in turbulent flow for Reynolds numbers at the orifice between 17,500 and 77,200. Three different sizes of orifice were used. The results from PIV were compared with the CFD simulations, with both global and local validations being performed. The former focusses on the pressure drop across the Sonolator and the latter was carried out by comparison of local values of velocity magnitude, turbulent kinetic energy and local specific turbulent energy dissipation rate. Velocity magnitude values were found to agree within 10% more than fifteen millimetres downstream of the orifice. A similar level of agreement was found at the orifice for lower flow rates and larger orifices. Factors which precluded this level of agreement for higher flow rates and smaller orifices were the appearance of cavitation and a minimum achievable laser pulse separation, limiting the maximum velocity measureable by the PIV. Agreement between PIV and CFD was also poorer for the turbulent parameters, although the PIV and CFD data had similar trends, the magnitudes were different. The reasons for these discrepancies include the fact that the oscillation period for the orifice jet could not be precisely identified and eliminated from the data and errors inherent in the methods used to estimate the local specific turbulent energy dissipation rate from the PIV data.

1. Introduction

The Sonolator is an inline mixer in the liquid whistle category (ex Sonic Corp, USA). The device is operated by passing multiphase fluids at high pressure through a cats-eye shaped orifice and over a blade; the device is used for mixing, emulsification, deagglomeration and disinfection in the manufacture of a range of products and intermediates in the home and personal care and fine chemicals industries. A schematic of the basic features of this mixer is given in Fig. 1, which enables identification of the expected mechanisms of fluid disruption as either due to energy dissipation across the orifice, or the impact and splitting of the fluid by the blade, both of which may induce cavitation.

To date, there is sparse information in the open literature about any aspect of the Sonolator or of liquid whistles in general; of the works that exist only a few accounts of industrial applications can be found (Clark et al., 2001; Chand et al., 2007). In particular, investigations into the interior workings of the Sonolator to determine the dynamics of the fluid motion, and how these define the performance of the device have not been documented.

The commonplace use of particle image velocimetry (PIV) and computational fluid dynamics (CFD) to measure and model industrial flows over the last two decades, respectively, have been made possible by the increase in computational power and advances in

* Corresponding author.
E-mail address: m.j.simmons@bham.ac.uk (M.J.H. Simmons).

http://dx.doi.org/10.1016/j.ces.2017.01.035
0009-2509/

Nomenclature

k	turbulent kinetic energy (J kg^{-1} or m^2 s^{-2})
M	mass flow rate (kg s^{-1})
ΔP	pressure drop over Sonolator (subscript of CFD, PIV, OUT is the data source)
u, v, w	X, Y, Z components of velocity vector field (m s^{-1})
u_{orif}	orifice superficial velocity (m s^{-1})
X, Y, Z	mutually orthogonal axes
x, y, z	coordinates as measured from orifice in the three axis directions (m)

Greek symbols

ε	epsilon, local specific turbulent energy dissipation rate (W kg^{-1} or m^2 s^{-3})
ε_{de}	epsilon derived from direct evaluation (DE) method (W kg^{-1})
ε_{sgs}	epsilon derived from sub-grid scale (SGS) method (W kg^{-1})

Abbreviations/glossary

0037	orifice of size 0.0037 in^2 (2.39 mm^2)
0110	orifice of size 0.0110 in^2 (7.10 mm^2)
0140	orifice of size 0.0140 in^2 (9.03 mm^2)
1D, 2D, 3D	one, two, three dimensional
BLOUT	blade-out Sonolator geometry
BLDIN	blade-in Sonolator geometry
CFD	computational fluid dynamics
DE	direct evaluation (method of deriving ε from PIV velocity gradients)
Delaunay	a meshing technique used within CFD, based on Delaunay triangulation
LDV	laser doppler velocimetry
Octree	a meshing technique used within CFD, based on subdividing cubes
OUT	denoting 'Outlet Hose' for pressure drop over the outlet hose
PIV	particle image velocimetry
Re	Reynolds number (subscript denotes the position, e.g. inlet, orif (orifice), MC (main chamber)
SGS	sub-grid scale (method of deriving ε from PIV velocity gradients)
SST-SAS	turbulence model in transient CFD
TKE	turbulent kinetic energy (denoted k, with units m^2 s^{-2})
XYZ	the whole flow domain including X, Y and Z axes
ZX	a plane defined by Sonolator axis (Z) and orifice long diameter (X)
ZY	a plane defined by Sonolator axis (Z) and orifice short diameter (Y)

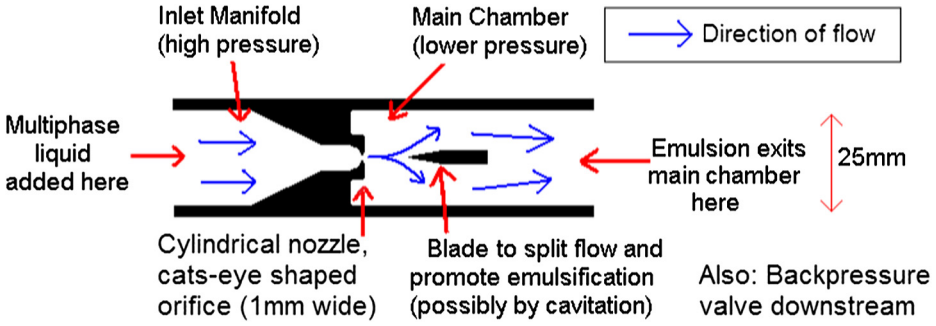

Fig. 1. Schematic diagram of Sonolator, showing orifice, blade and main chamber.

digital imaging. Many combined PIV/CFD investigations now exist and are especially desirable: PIV provides reliable experimental data but is time-consuming and expensive; CFD requires validation but is cheap relative to PIV (Nakiboğlu et al., 2009), hence CFD can generate a wider range of results for the same financial investment once its reliability is proven. Individual CFD simulations can be compared with corresponding experiments (such as PIV) and obtaining the required good agreement between the results. When agreement is obtained over a set of experiments covering a range of flow conditions then the CFD can be regarded as validated over that range, and future investigations of the same type can be carried out via CFD alone provided that no significant alterations are made to the modelling assumptions.

Some examples of successful PIV/CFD comparisons for industrial applications have a wide scope and include: a rotating disc contactor extractor column (Drumm and Bart, 2006), silicone elastomer models of cerebral aneurysms (Ford et al., 2007), flow through a rough microchannel (Silva et al., 2008), pollution monitoring of an isolated smoke stack in an atmospheric boundary layer (Nakiboğlu et al., 2009), a fluidised bed (Hernández Jiménez et al., 2011), two phase natural convection (Gandhi et al., 2011) and a 1.2 MW moving grate combustion boiler (Nussbaumer and Kiener, 2013).

Focusing on applications of PIV/CFD comparisons to confined turbulent flows; suitable comparisons may be found for pumps, stirred tanks, and multiphase jet flows. PIV/CFD comparisons were carried out for a radial pump in the impeller and diffuser regions (Feng et al., 2009) and for a centrifugal pump impeller (Westra et al., 2010). In both cases the main method of comparing velocities was to plot PIV and CFD results together on a line graph, with velocity on the vertical axis, and distance along a line in the flow domain on the horizontal axis (also used in Nakiboğlu et al., 2009; Drumm and Bart, 2006). The PIV and CFD velocities demonstrated good agreement, in one paper (Westra et al., 2010) the velocities agreed to within 5%. Turbulence fields were also compared by Feng et al. (2009) using graphs of turbulent intensity *vs* distance; the trends were the same in CFD and PIV, but with the magnitude underestimated in CFD (also see Nakiboğlu et al., 2009, where greater variation was found for turbulence than for velocity comparisons). In addition, LDV was found to give better turbulence readings at a point than PIV for geometries where PIV was adversely affected by planar reflections of the laser sheet.

PIV/CFD comparisons were carried out for a stirred tank with a pitched blade turbine and baffles by Sheng et al. (1998) and for a Rushton turbine with baffles (Ranade et al., 2001). In both cases the CFD was for fully developed flow using steady-state simulations, with boundary conditions at the turbine being modelled with suction and ejection of fluid. The PIV work was not angle resolved for Sheng et al. (1998), but was angle resolved in the later work (Ranade et al., 2001). For turbulence models, Sheng et al. used RNG k-ε and RSM, whereas Ranade et al. used standard k-ε and RNG k-ε. In both cases, graphs of velocity *vs* distance (along various lines in the flow domain) were used to demonstrate agreement between PIV and CFD, with comparable results across all turbulence models (and no additional accuracy when using the more computationally intensive RSM). Turbulence was also plotted on line graphs; for Sheng et al. where there was qualitative agreement between CFD and PIV of the general pattern of turbulence; for Ranade et al. the standard k-ε model gave good agreement but only after deducting the periodic component of kinetic energy caused by the regular passage of the turbine blades.

Virdung and Rasmuson (2007) compared PIV and CFD measurements for a confined solid-liquid jet. The PIV was carried out using matched refractive indices between solid and liquid phases, and results were obtained up to a solid loading of 1.9 vol%; the accuracy decreased as the solid loading increased. The CFD used a realisable k-ε turbulence model which was varied between mixture, dispersed and per-phase applications; the latter gave best agreement to PIV, demonstrated by graphs of velocity *vs* distance using both data sources.

To summarise, PIV/CFD comparisons have been successfully carried out for many industrial applications. Velocity fields between PIV and CFD tend to agree in pattern and magnitude; whilst turbulence fields tend to agree in pattern but not in magnitude. Care ought to be taken when calculating turbulent fields to deduct (where possible) any contribution from periodic motion. Using more complex turbulence models (e.g. RSM over RANS) has not resulted in superior validation to date.

This paper describes a series of novel PIV experiments carried out to determine the single phase flow field within the main chamber of a Sonolator liquid whistle over a range of industrially relevant flow conditions; the effect of orifice size, the presence of the blade and the mass flow rate are explored. These experiments were carried out to elucidate the features of the flow which impact upon the performance of the device in terms of its use as an emulsification device. The results are then compared with simulations carried out using CFD to assess the capability of the CFD to accurate represent the measured flow phenomena, given the observed complexity of the flow field and high velocity gradients measured (Ryan et al., 2011, 2013).

2. Materials and methods

2.1. Sonolator geometry and flow conditions for PIV and CFD

Six Sonolator geometries were investigated, based on a Model A Sonolator using three orifice sizes, (designated 0037, 0110, 0140, see Table 1 for dimensions) and two blade configurations (designated BLDIN for Blade-In, and BLOUT for Blade-Out). The (0110, BLDIN) geometry combination is illustrated in Fig. 2; the other geometry configurations were obtained through altering the orifice size or removing the blade from the flow domain.

Table 1 shows the flow conditions used in the investigation. The input parameters were orifice size, blade presence/absence, and mass flow rate. The experiments were carried out at fixed pressure drop across the orifice, as specified by the set controller on the pump. Initial investigations found little influence of the blade, but unsurprisingly a substantial effect due to orifice size. Hence, different mass flow rates were investigated for different orifice sizes. Note that the calculated Reynolds numbers were over 17,000 at the orifice, (Re_{orif}) indicating fully turbulent flow and the flow remained turbulent in the main chamber downstream ($Re_{MC} > 2500$). As shown later, this agreed with the turbulent eddy patterns directly observed in the PIV images.

For each orifice size, experiments were conducted at low and high mass flow rates, for both blade in and out, giving six conditions in total in Table 1. For the medium size orifice, a medium flow rate was also investigated. (The precise mass flow rates were orifice dependent, see Table 1.) In the results presented below, generally the medium case will be presented first, with a montage of the six other cases afterwards, to aid CFD and PIV comparisons over a range of conditions.

2.2. PIV experiments for the Sonolator

A transparent mimic of the Model A Sonolator (ex. Sonic Corp, USA) was built to enable PIV measurement of flow fields inside. The volume of interest was the main chamber of the Sonolator directly downstream from the orifice. Since the main chamber walls were solid metal, optical access was needed for the PIV laser and camera. This was enabled by replacing the metal main chamber walls with a cuboid Perspex section, the internal flow cavity milled to the same cylindrical geometry as the original Sonolator, with the external faces made flat and perpendicular to both laser and camera. This allowed optical access to the area directly after the orifice, in two orientations; the flat external faces and close refractive indices of both Perspex and water meant that no distortions were visible in the images. A removable blade was also constructed to have similar geometry to the original. A drawing of the PIV experimental

Table 1
Descriptions of setups investigated in PIV experiments and CFD simulations.

Orifice and blade	Low flow rate	Medium flow rate	High flow rate
0037 0.0037 in^2 (2.39 mm^2) (BLDIN and BLOUT)	M = 0.036 kg s^{-1} u_{orif} = 15.2 m s^{-1} Re_{inlet} = 4200 Re_{orif} = 26,500 Re_{MC} = 1500		M = 0.091 kg s^{-1} u_{orif} = 38.4 m s^{-1} Re_{inlet} = 10,500 Re_{orif} = 66,700 Re_{MC} = 3700
0110 0.0110 in^2 (7.10 mm^2) (BLDIN and BLOUT)	M = 0.046 kg s^{-1} u_{orif} = 6.5 m s^{-1} Re_{inlet} = 5300 Re_{orif} = 19,600 Re_{MC} = 1900	M = 0.092 kg s^{-1} u_{orif} = 12.9 m s^{-1} Re_{inlet} = 10,500 Re_{orif} = 38,800 Re_{MC} = 3800	M = 0.182 kg s^{-1} u_{orif} = 25.8 m s^{-1} Re_{inlet} = 20,900 Re_{orif} = 77,200 Re_{MC} = 7500
0140 0.0140 in^2 (9.03 mm^2) (BLDIN and BLOUT)	M = 0.047 kg s^{-1} u_{orif} = 5.2 m s^{-1} Re_{inlet} = 5400 Re_{orif} = 17,500 Re_{MC} = 1900		M = 0.182 kg s^{-1} u_{orif} = 20.3 m s^{-1} Re_{inlet} = 21,000 Re_{orif} = 68,500 Re_{MC} = 7500

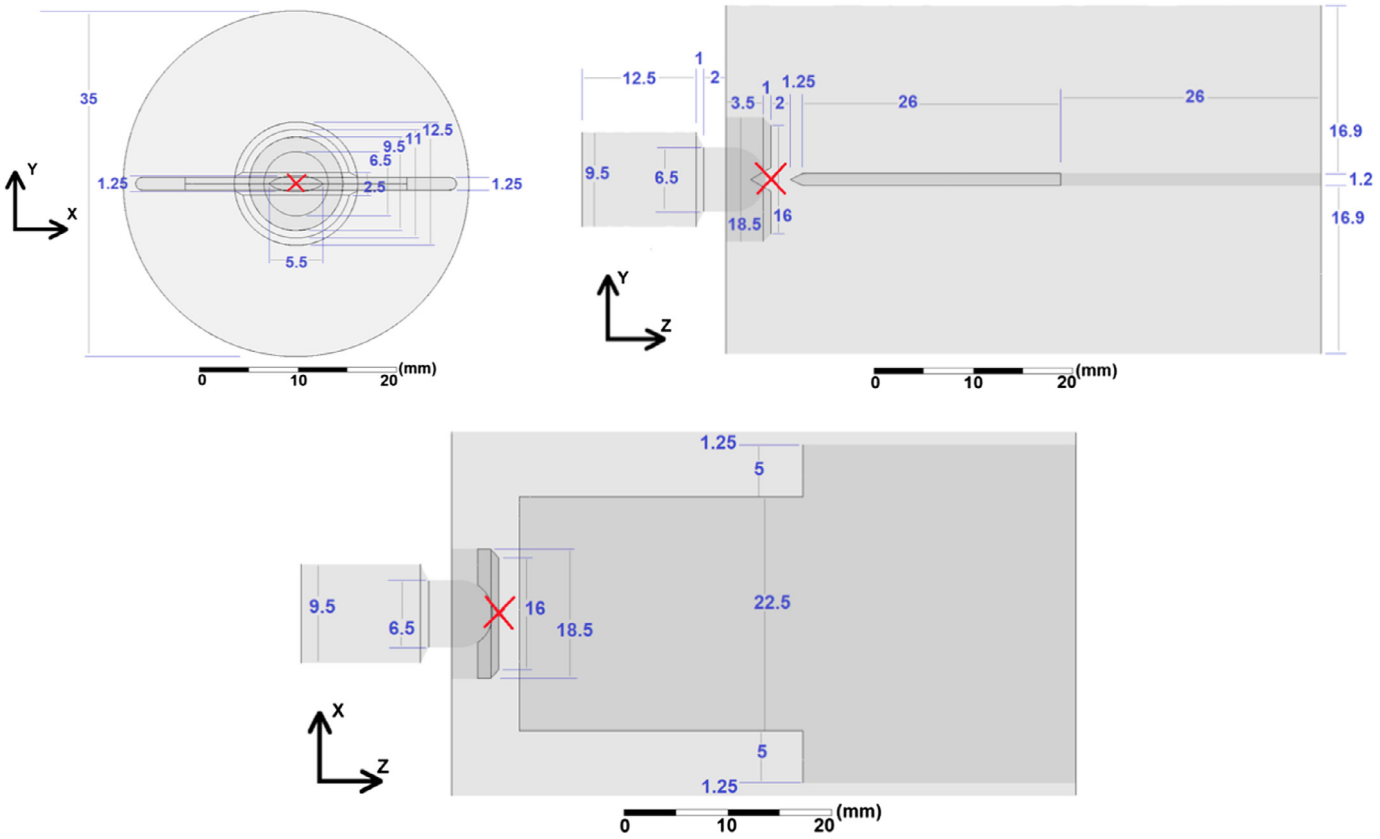

Fig. 2. Geometry of Sonolator flow domain in XY, ZY, ZX planes; 0110 orifice, blade in. Red cross is position of origin $(x, y, z) = (0, 0, 0)$. (For interpretation of the references to colour in this figure legend, the reader is referred to the web version of this article.)

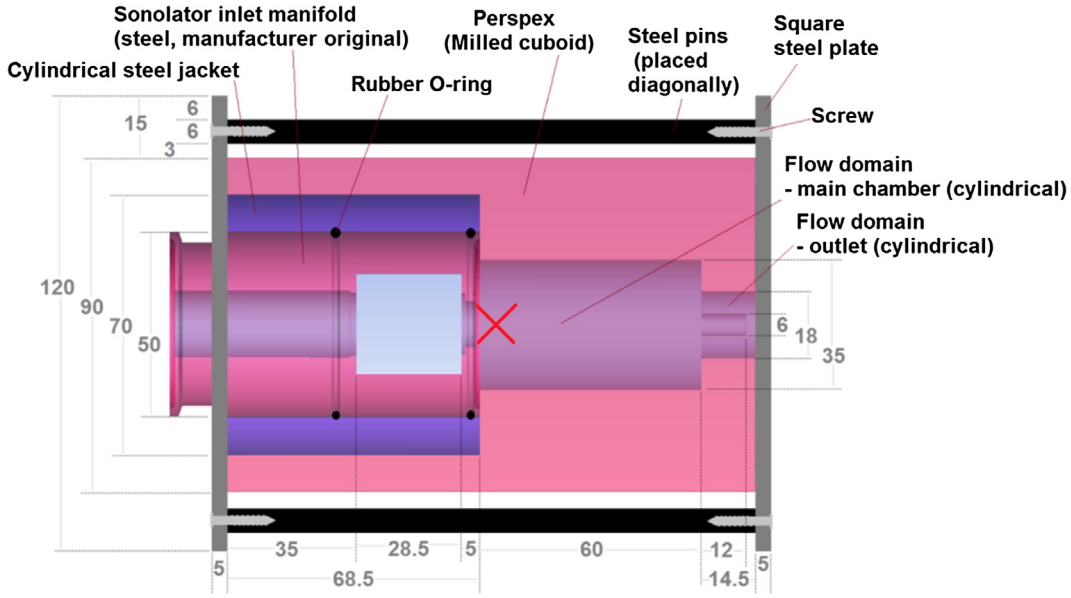

Fig. 3. Drawing of Sonolator assembly (minus orifice) in axial (Z) and vertical (Y) directions, with dimensions given in millimetres. The coordinate origin ($y = 0, z = 0$) has been marked with a red cross, which is 4.5 mm to the right and 17.5 mm above the bottom left corner of the flow domain. The light blue gap to the left of coordinate origin housed one of the three orifices during experiments. (For interpretation of the references to colour in this figure legend, the reader is referred to the web version of this article.)

apparatus including dimensions is given in Fig. 3, and a photograph of the assembly used for experiments is shown in Fig. 4.

The 2-D PIV measurements were performed using a TSI PIV system (TSI Inc, Shoreview, MN., USA) comprised of a 532 nm Nd-Yag 50 mJ per pulse dual-head laser (New Wave Solo III, ex. New Wave Research, Fremont, CA., USA) pulsing at 7 Hz, synchronized to a single TSI Powerview 4MP (2048×2048 px^2) 12 bit grayscale frame-straddling CCD camera using a synchronizer (TSI 610035) attached to a Dell Precision 620 workstation. The PIV system was controlled using TSI Insight 4G software, which stored the PIV images and carried out the cross-correlation described below which extracted the velocity vectors of the flow from the data.

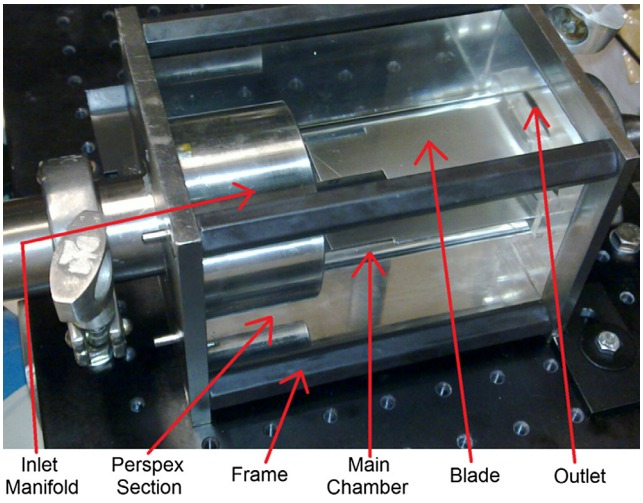

Fig. 4. Photograph of experimental Sonolator rig.

The working fluid for PIV experiments was mains water at ambient temperature and pressure. Recorded temperatures were within the range 22–27 °C. The working fluid was stored in a tank of volume 60 L and recirculated through the experimental apparatus as shown in Fig. 5. Seeding particles were added to the working fluid for PIV imaging. The particles chosen for this study were 10 μm silver coated hollow glass spheres which were neutrally buoyant in water. They were found to give good reflectivity under the laser sheet, being clearly visible on the image at an added concentration of 0.0083 g L^{-1}. The relaxation time was checked; the Stokes number reached a maximum near the orifice of 0.212, 0.071 and 0.051 for orifices 0037, 0110 and 0140 respectively; during these experiments the Stokes number was much less than unity indicating these particles followed the flow faithfully. The concentration of particles used was increased in each PIV experiment until the optimal number of particles, on average 15 (Keane and Adrian, 1991), were found in each interrogation area of 32 px × 32 px on the resulting PIV exposures.

PIV image exposures were obtained for blade out (BLOUT) in both ZY and ZX planes (see Fig. 2 above), but for blade in (BLDIN) only in ZY plane, since the ZX plane was blocked by the blade. For each measurement 500 image pairs were captured, a large enough number to demonstrate convergence of average values for planar (2D) velocities in the 2D measurement plane.

Fig. 6 shows an example of a set of velocity measurements in the ZY plane, with the blade out. Turbulent k and ε flow fields could also be estimated from the velocity variance and gradients using the equations below (adapted from Gabriele et al., 2009; Gabriele et al., 2011). In these equations (u, v, w) are the (x, y, z) components of velocity using Cartesian coordinates. An isotropic assumption has been used to substitute for the velocity component u which

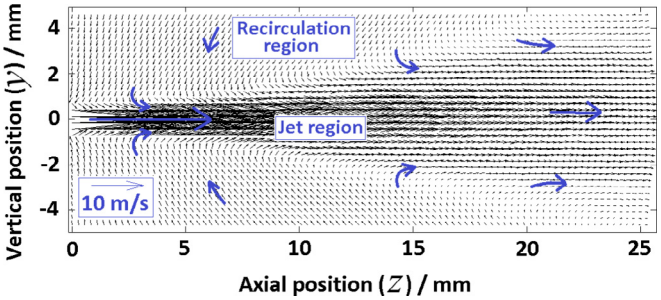

Fig. 6. Vector plot of time-averaged velocity (ZY plane, medium orifice (0110), blade out, medium flow rate of 0.092 kg s^{-1}).

was missing in the ZY plane. Gabriele et al. (2009) gave two versions of ε, both of which are used in this paper: direct evaluation (ε_{de}) which tends to underestimate due to the PIV grid scale being larger than the smallest turbulent eddies and thus acting as a cut-off, and a sub-grid scale model (ε_{sgs}) which adds back in the estimated effect of the unmeasured small eddies.

$$k = \frac{3}{4}(\tilde{v} + \tilde{w}) \tag{1}$$

$$\varepsilon_{de} = \upsilon_C \left[2\overline{\left(\frac{\partial w'}{\partial z}\right)^2} + 2\overline{\left(\frac{\partial v'}{\partial y}\right)^2} + 3\overline{\left(\frac{\partial w'}{\partial y}\right)^2} + 3\overline{\left(\frac{\partial v'}{\partial z}\right)^2} + 2\overline{\frac{\partial w'}{\partial y}\cdot\frac{\partial v'}{\partial z}} \right] \tag{2}$$

(υ_c is the continuous phase kinematic viscosity, the prime $'$ represents a variable minus its time-averaged value)

$$\varepsilon_{sgs} = (C_S\Delta)^2 \left[4\overline{\left(\frac{\partial w'}{\partial z}\right)^2} + 4\overline{\left(\frac{\partial v'}{\partial y}\right)^2} + 2\overline{\left(\frac{\partial w'}{\partial y}\right)^2} + 2\overline{\left(\frac{\partial v'}{\partial z}\right)^2} \right]^{3/2} \tag{3}$$

(C_s is the Smagorinsky constant, estimated at 0.17, and Δ is the grid scale which was approximately 0.27 mm.)

ZX-plane PIV images were also attempted. In Fig. 6 (for ZY plane) the orifice jet is seen to be less than 1.5 mm across at the thinnest point. Hence for PIV in the ZX-plane it was estimated that the laser sheet would need to be positioned with accuracy of order 0.1 mm in order to capture the exact centre of the orifice jet. This accuracy in positioning was not achievable in practice, the achieved positioning accuracy was of order 0.2 mm, hence the ZX-plane data tended to fall outside the exact centre of the jet and was not accurate enough to provide good comparison. Thus in the analysis below the ZY-plane data is used exclusively to compare with the CFD.

2.3. CFD simulations for the Sonolator

CFD simulations were carried out using ANSYS CFX software to match the PIV experiments described above. This software used a

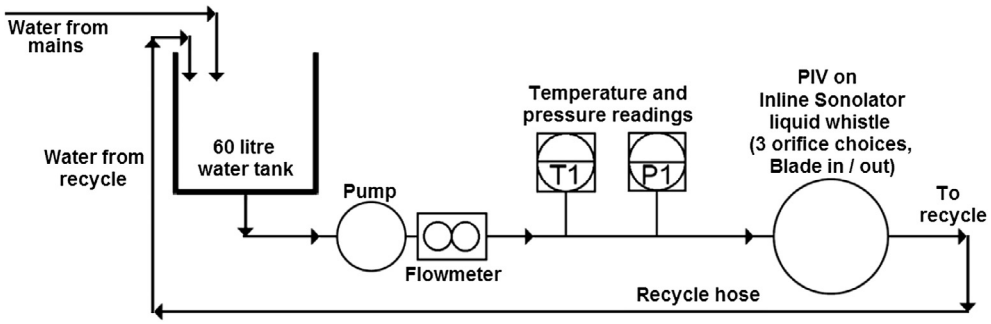

Fig. 5. Diagram of experimental setup surrounding the PIV rig.

finite volume method to convert the Navier-Stokes equations governing fluid flow within the Sonolator into volume integrals over a finite mesh. Single phase water flow was specified since this corresponded to the PIV experimental condition. Minimal heating was found during the PIV experiments, so for CFD a fixed temperature of 25 °C was used, and heat transfer was not simulated. Transient simulations were used since during PIV a variable jet direction was found.

Since direct numerical simulation was intractable, the turbulence model of SST-SAS was chosen. SST is a blend of k-omega near the wall, and k-epsilon in the free stream, using each turbulence model in locations to which it is best suited. SAS adds transient simulation of the most important turbulent eddies, and is a variant of DES which eliminates dependence on grid spacing. SST-SAS is recommended in the literature for transient turbulence modelling on industrial machinery, see Menter (1993, 1994), Egorov and Menter (2008), Egorov et al. (2010).

ANSYS ICEM was used to generate the geometry corresponding to the PIV experiments, and to mesh its 3D volume. The two mesh generation methods available were Delaunay and Octree. Delaunay was based on the 3D analogue of planar Delaunay triangulation methods. Octree was based on creating a cubic mesh, splitting individual cubes into tetrahedra, then mapping these to any adjacent surfaces and clipping the resulting tetrahedral mesh appropriately. Using both meshing techniques helped to ascertain mesh independence of the results, since these two methods gave unrelated meshes.

Mesh independence tests were carried out for both mesh generation methods. Mesh fineness was investigated by increasing its density by integer powers of two, thus three different mesh densities were investigated for each, denoted 'low', 'medium' and 'high' density. The number of elements ranged from 200 k for the low density mesh to 1.5 M for the high density mesh. Prism layers were used on all wall surfaces for both techniques, since this allowed the large velocity gradients to be resolved near the walls.

Velocity magnitudes along the Sonolator axis were compared for each of the 6 meshes. The medium and high density meshes gave similar results, and the low quality mesh gave noticeably worse results due to insufficient mesh density in the high velocity regions such as directly after the orifice. From this, the medium density meshes were judged suitable for the final simulations and are shown in Fig. 7. Full details of this comparison are given in Ryan (2015); the medium density Octree mesh was used to generate the simulations due to its lower computational cost compared with the Delaunay mesh.

Overall both initial state and transient simulation had a high degree of convergence. All transient simulations were initialized on a converged result from an initial simulation where residuals were $<10^{-5}$. For the transient simulations, at each time step it was necessary to iterate to converge the residuals to a low level. Each iteration was called a "coefficient loop". Between 1 and 10 coefficient loops were used to reduce all residuals of velocity, mass and turbulence variables below 10^{-4}.

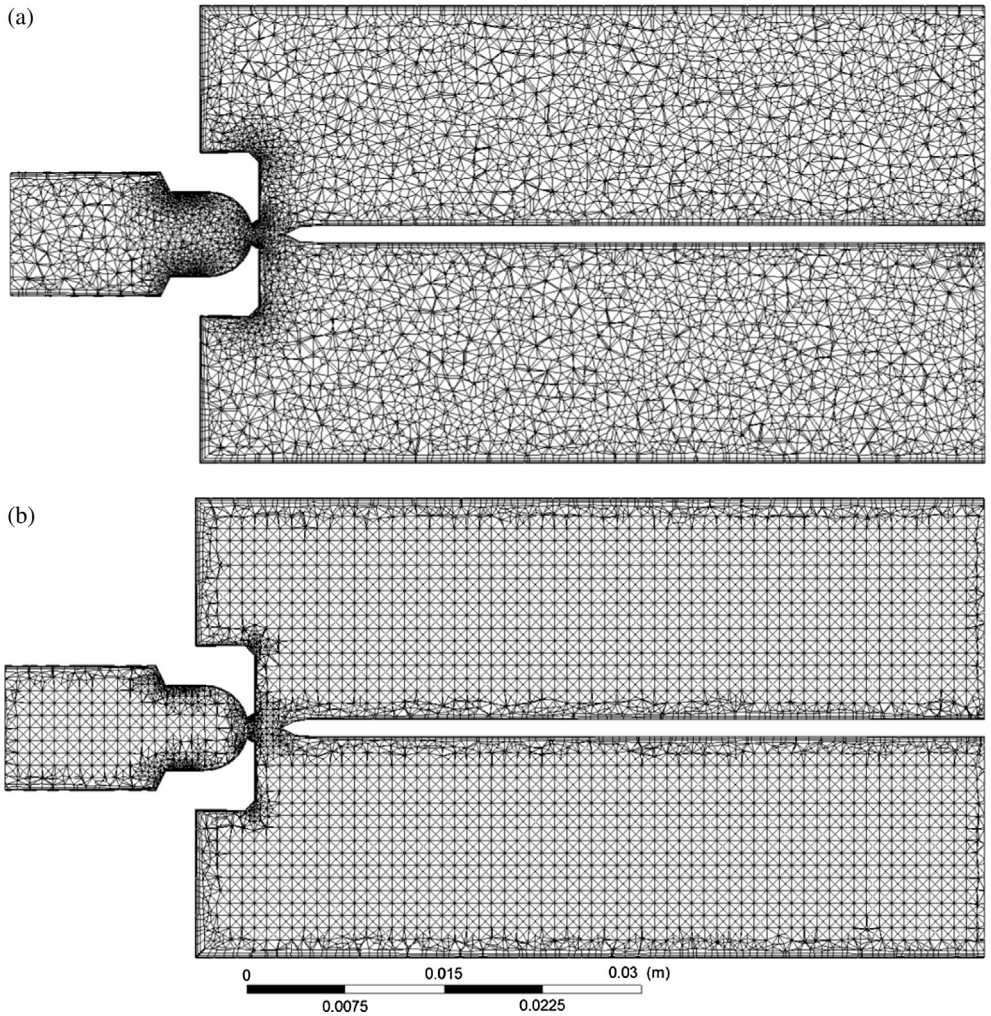

Fig. 7. Section in ZY plane through medium density Delaunay (a) and Octree (b) meshes with prism layers for 0110 orifice, Blade In.

Three boundary conditions were applied: inlet, outlet and wall. Over the Sonolator inlet, the mass flow rate was fixed to correspond to the relevant PIV experiment. At the outlet a fixed pressure of 1 atm or 101,325 Pa was specified. Every other boundary of the flow domain was designated a wall, which was a stationary smooth surface with a no-slip condition.

ANSYS software allowed processing with single or multiple cores (serial or parallel processing); the results were found to be independent of the number of cores, so between 4 and 16 cores were used in parallel for the final results.

In PIV the results were time averaged from at least 500 frames; both average and fluctuating velocity (root mean square) measurements were checked successfully for stability. The CFD solver provided time-averaged values for the following flow variables: static and dynamic pressure, each of the three components of velocity in Cartesian co-ordinates, turbulent kinetic energy, turbulent dissipation rate. Typical results are given in Fig. 8 above, where for medium flow rate and medium orifice size the velocity fields are compared in two planes (ZY, ZX) and for blade in/out. One-dimensional cross-sections through velocity fields like these were used to compare CFD to PIV, in order to validate the CFD.

2.4. Comparison methodology

The CFD data were fully 3-D, however the PIV velocity data were planar. During PIV, in-plane velocity components were obtained for two planes (ZY, ZX) through the Sonolator flow field. These were both symmetry planes of the Sonolator device. Moreover, the time-averaged measurements were found to be symmetric in both of these planes (e.g. see Figs. 6, 8 above); this was since asymmetric temporal fluctuations, such as those due to turbulence, would be expected to cancel out on average. For all PIV velocity measurements, the velocity component normal to the plane of the thin (<1 mm) laser sheet was negligible, and the velocity magnitude could be calculated accurately from the two measured in-plane components.

An advantage of using velocity magnitude, rather than the velocity components, was that it was positive definite and so could be plotted on a log-scale. Since velocity varied over several orders of magnitude throughout the flow domain, use of a log-scale meant the same graph could meaningfully compare velocities which were both large and small in different locations. The same reasoning was also held for the turbulent fields.

For comparing PIV and CFD, flow variables (velocity or turbulence) were plotted on various one-dimensional lines through the flow domain. These were either the axial line or various cross-sectional lines at different distances from the orifice, see Fig. 9 for an illustration of these lines in the ZY plane for blade out.

3. Results and discussion

3.1. Pressure drop

During PIV, mass flow rate was fixed for each individual experiment and pressure drop across the Sonolator measured; for corresponding CFD simulations, the same mass flow rates were inputted and in each case pressure drops outputted. The results obtained are shown in Table 2. Note that the data below are for blade-out only, since adding the blade was found to increase the pressure drop by a negligible amount in either PIV or CFD. Also dynamic and static pressure results agreed due to relatively low flow speed at inlet/outlet.

In Table 2 the CFD pressure drop as a percentage of the PIV pressure drop is given. Since the CFD does not simulate the outlet pipe, which is included in the experimental pressure drop, thus additional term (ΔP_{OUT}) has been calculated assuming that the pipe is smooth using the Darcy-Weissbach equation. The CFD pressure drops gave predictions between 89% and 106% of the true pressure drop from PIV experiments, a reasonable agreement.

3.2. Comparison of velocity magnitudes: Sonolator (Z) axis, blade-out

The seven experimental setups given in Table 1 have one middle case (0110 orifice, 0.092 kg s^{-1}) and six "edge" cases, of which

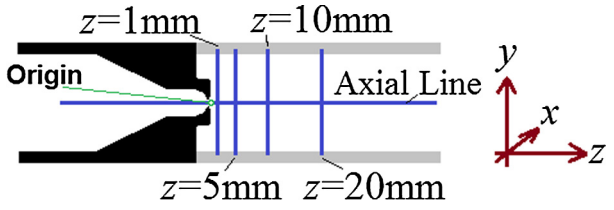

Fig. 9. Schematic diagram showing lines in the ZY plane along which PIV and CFD results were compared. For PIV, black regions were metal (opaque), grey regions were Perspex (transparent).

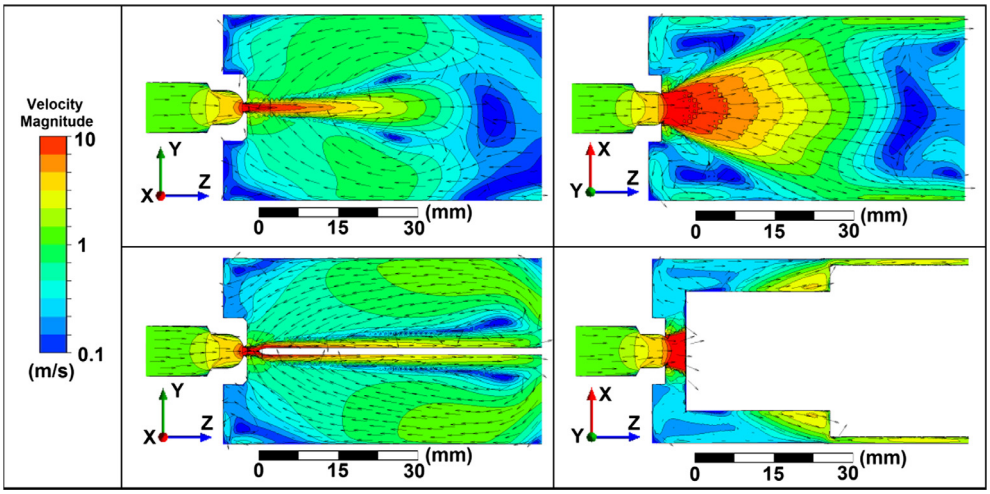

Fig. 8. Contour plots in ZY (left) and ZX (right) planes of time-averaged velocity magnitude for blade-out (upper) and blade-in (lower) cases (2 × 2 grid). Vectors showing direction (but not magnitude) superimposed. Medium case (0110 orifice, 0.092 kg s^{-1} mass flow rate).

Table 2
Pressure drop results from PIV and CFD for blade-out experiments/simulations, at 7 different mass flow rates and using 3 different orifices. Mass flow rates (M), orifice superficial velocities (u_{orif}) also given.

Orifice size code	M (kg s^{-1})	u_{orif} (m s^{-1})	ΔP_{PIV} (kPa)	ΔP_{CFD} (kPa)	ΔP_{OUT} (kPa)	$(\Delta P_{CFD} + \Delta P_{OUT})/\Delta P_{PIV}$ (%)
0037	0.036	15.2	172.4	152.2	1.22	88.99
0037	0.091	38.4	1094	952.6	6.19	87.64
0110	0.046	6.5	34.5	32.1	1.87	98.48
0110	0.092	12.9	137.9	125.7	6.30	95.72
0110	0.182	25.8	540.1	496.3	20.80	95.74
0140	0.047	5.2	20.7	19.9	1.95	105.54
0140	0.182	20.3	326.4	304	20.80	99.51

three had low flow rates (0.036–0.047 kg s^{-1}) for their respective orifices, and three had high flow rates (0.091–0.182 kg s^{-1}). CFD and PIV will be compared for the middle case first, then montages illustrating the six edge cases. The first location for comparison is the axial line (Z axis) shown in Fig. 9. Since at this location data was not available for blade-in cases (due to the blade occupying most of the axis) blade-out data is given. Although CFD data was available for all values of z, for PIV, data was only obtainable for $z > 0$ (Fig. 4) due to the opaque metal orifice blocking optical access.

In Fig. 10 velocity magnitudes are given for CFD (2 meshes) and PIV along the Sonolator axis (the line $x = y = 0$ mm, with z the position parameter). Both CFD and PIV showed a peak in velocity of magnitude 17 m s^{-1} about 1 mm after the orifice in the jet region, and a subsequent exponential decline (a straight line on this log-scale graph) in velocity magnitude with distance along the Sonolator.

After 15 mm from the orifice (which was at $z = 0$ mm on the horizontal scale), the PIV results were in-between the two CFD data; between 0 mm and 15 mm the PIV results were slightly higher than the CFD results. Overall, for this middle orifice size and flow rate, the agreement between CFD and PIV was very good, and the velocity magnitude was validated in this case. In Fig. 11 the same data is viewed in a montage for the edge cases.

Fig. 11 shows a common feature of all datasets was good agreement between CFD and PIV after $z = 15$ mm with an exponential decline in velocity with position. For three cases (0140 low and high flow rates, 0110 low flow rate) the agreement between CFD and PIV was good enough to provide a complete validation of CFD results along the whole axial line.

In the other three cases before $z = 15$ mm, discrepancies between PIV and CFD were found. For 0037 orifice at low flow rate a source of PIV inaccuracy in high velocity regions was that the laser pulse separation could not be reduced sufficiently to capture the high velocity flows correctly; a minimum pulse separation of 5 μs and minimum interrogation area of 32 × 32 px were required for reliable PIV processing. For 0037 and 0110 orifices at high flow rate, cavitation was observed visually on the PIV images in the high velocity regions. Both these reasons prevented gathering of accurate PIV data in the same region, and will be observed on subsequent jet cross-sections for both blade-in and blade-out. So the question posed is can the remaining CFD cases be validated by other arguments?

For 0110 orifice: the CFD region was validated in both cases ($z \geqslant 15$ mm) indicated that velocity magnitude was proportional to the flow rate. The flow rate ratio was 4 between low and high flow rates, hence the velocity patterns everywhere should also scale with a ratio of 4. This is indeed observed along the whole Sonolator axis. Hence by a scaling argument, the CFD results for 0110 orifice, high flow rate, were valid along the whole Sonolator axis.

The 0037 orifice results were slightly harder to validate: for high flow rate after $z = 15$ mm there was good agreement; for low flow rate after $z = 15$ mm there was agreement in the velocity pattern, but a slight discrepancy in the magnitude. Moreover in the unvalidated region ($z < 15$ mm) there was no accurate PIV data obtainable for 0037 orifice. Comparing CFD patterns for 0037 orifice with larger orifices, the peak velocity shape for 0037 orifice (both meshes) was similar to that of the larger orifices for Delaunay mesh. This gave some confidence that the 0037 CFD results were physical.

The arguments above support the conclusion that the velocity magnitude calculated by the CFD on the Sonolator axis was valid across all orifices and flow rates. Next, the jet cross-sections are examined to see if the same conclusion can be drawn.

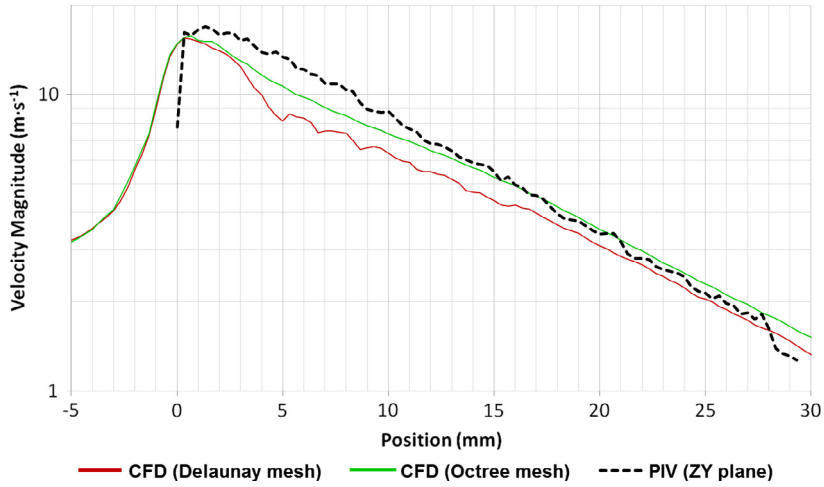

Fig. 10. Graph of velocity magnitude along the axial line (Z axis). CFD and PIV results compared for blade-out middle case (0110 orifice, 0.092 kg s^{-1}). Reference data: Sonolator pressure drop 125.7 kPa for CFD, orifice superficial velocity 12.9 m s^{-1}, main chamber superficial velocity 0.1 m s^{-1}.

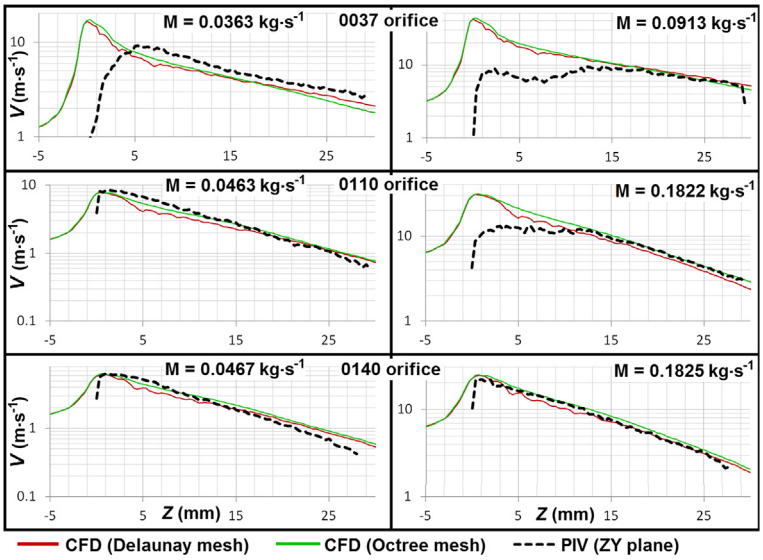

Fig. 11. Montage of graphs of velocity magnitude along the axial line. CFD and PIV results compared for blade-out, all six edge cases (three orifice sizes from top to bottom, low/high flow rates from left to right.

3.3. Comparison of velocity magnitudes: ZY cross-sections (fixed Z, varying Y), blade-out

Edge-case montages of the orifice jet cross-section are given in Fig. 12 below for three different distances after the orifice (1 mm, 5 mm and 10 mm), each distance with a separate montage of six graphs for the orifices and flow rates investigated.

Fig. 12 shows PIV and CFD comparison of velocity magnitude for the orifice jet in cross-section, for three distances from the orifice, three orifice sizes and two flow rates. In Fig. 12a the same CFD cases as before (0110 orifice for low flow rate, 0140 orifice for low and high flow rates) can be immediately validated by their excellent agreement with the PIV data. In these cases, the peak velocity magnitude within the jet was seen to be around 10 times as large as mean velocity magnitudes in the recirculation regions surrounding the jet. The other two cross-sections are presented in Fig. 12b and Fig. 12c at 5 mm and 10 mm downstream of the orifice respectively both show good agreement between PIV and CFD for all cases except 0037 orifice size at high flow rate.

Overall the three jet cross-section montages show a wide range of agreement between CFD and PIV. The remaining discrepancies were almost all in places where issues with the PIV measurements had been identified, and reasons for believing CFD results in those areas were accurate included (i) scaling comparisons between low and high flow rates, and (ii) similarities found in flow patterns between different orifice sizes.

The axis and three cross-sections were subsets of the flow domain with a representative set of velocities and flow conditions. Hence the validation demonstrated above for these subsets was good evidence that velocities from CFD were valid across the whole flow domain for the blade-out edge cases considered above, or for interior CFD cases (e.g. medium flow rates, intermediate orifice sizes) carried out in future.

3.4. Comparison of velocity magnitudes: ZY cross-sections, blade-in

Having discussed the blade-out cases, attention is now turned to the blade-in cases, which represent normal industrial usage of the Sonolator. Since the Sonolator axis lies mostly outside the flow domain (and within the blade), only cross-section CFD/PIV comparisons are carried out here; as before, the comparisons are at z = 1 mm, 5 mm and 10 mm after the orifice.

Fig. 13a shows excellent agreement between CFD and PIV velocities in the jet region for the normal three cases (0110 low flow, 0140 low and high flow). The same three cases had PIV inaccuracy for reasons discussed above, although attention is drawn to some excellent agreement for 0037 case outside the jet region. Note, this case was just before the blade so PIV could be obtained above and below the blade.

In Fig. 13b PIV readings were only obtained for half the flow domain due to the opaque blade blocking light from the other half of the flow domain. Agreement in both split jet and recirculation regions was good, in some cases (0140, low flow rate) excellent. Likewise, in Fig. 13c agreement between PIV and CFD for both split jet and recirculation regions was good.

These results for the blade-in cases demonstrated that there was no decrease in accuracy of CFD simulation going from blade-out to blade-in cases; conversely, in many cases accuracy seemed to increase. In particular, the new feature of these simulations (the blade) was shown to be simulated accurately in CFD in terms of the velocity patterns obtained near it.

The overall conclusion for comparisons of velocity magnitude between CFD and PIV data was that the PIV data, where accurate, supported the CFD results, moreover that it was reasonable to believe the CFD velocities to be accurate everywhere in the flow domain, for both blade-out and blade-in simulations, within the scope of orifice sizes and flow rates discussed here. It also showed that the SST-SAS turbulence model used for CFD was suitable for obtaining accurate velocity fields in the Sonolator.

3.5. Comparison of turbulence parameters (k, ε)

In the previous sections, velocity fields between CFD and PIV were found to be in good agreement and in this section the agreement for the turbulence parameters is explored. Previous research (cited in the literature review) showed that it was more common for the pattern of turbulence to agree between PIV and CFD, than for the magnitudes to agree. It also found that PIV was not the most accurate technique for experimentally determining turbulence due to the relatively low temporal sampling frequency (LDV is more accurate); nevertheless the sample size (500 frame pairs) was sufficiently high to ensure convergence of the statistical turbulent parameters. This section will demonstrate that these problems of determining the turbulence fields have not been overcome by the

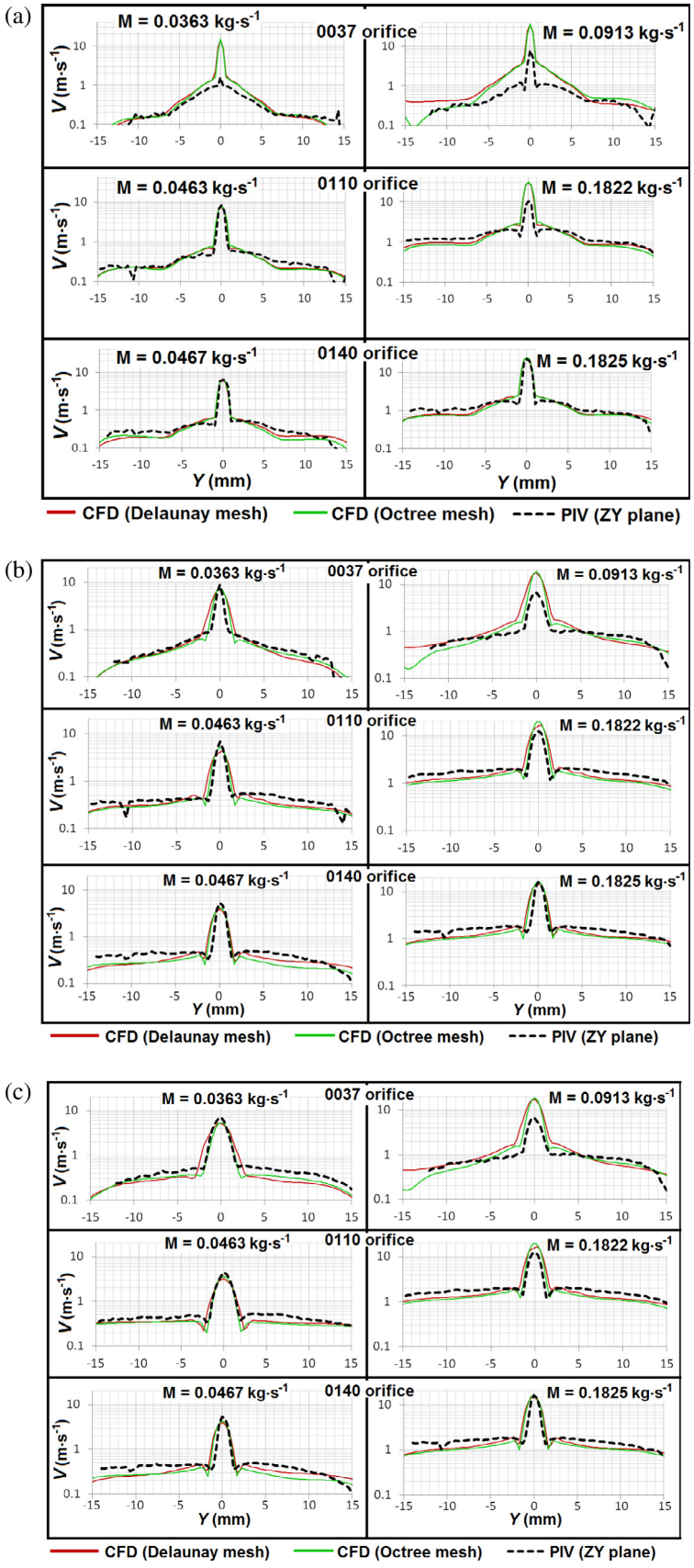

Fig. 12. Montages of graphs of velocity magnitude in ZY plane, blade-out. CFD and PIV results compared for all edge cases (low/high flow rates, orifices of types 0037, 0110, 0140) along lines at (a) $z = 1$ mm, (b) $z = 5$ mm, (c) $z = 10$ mm.

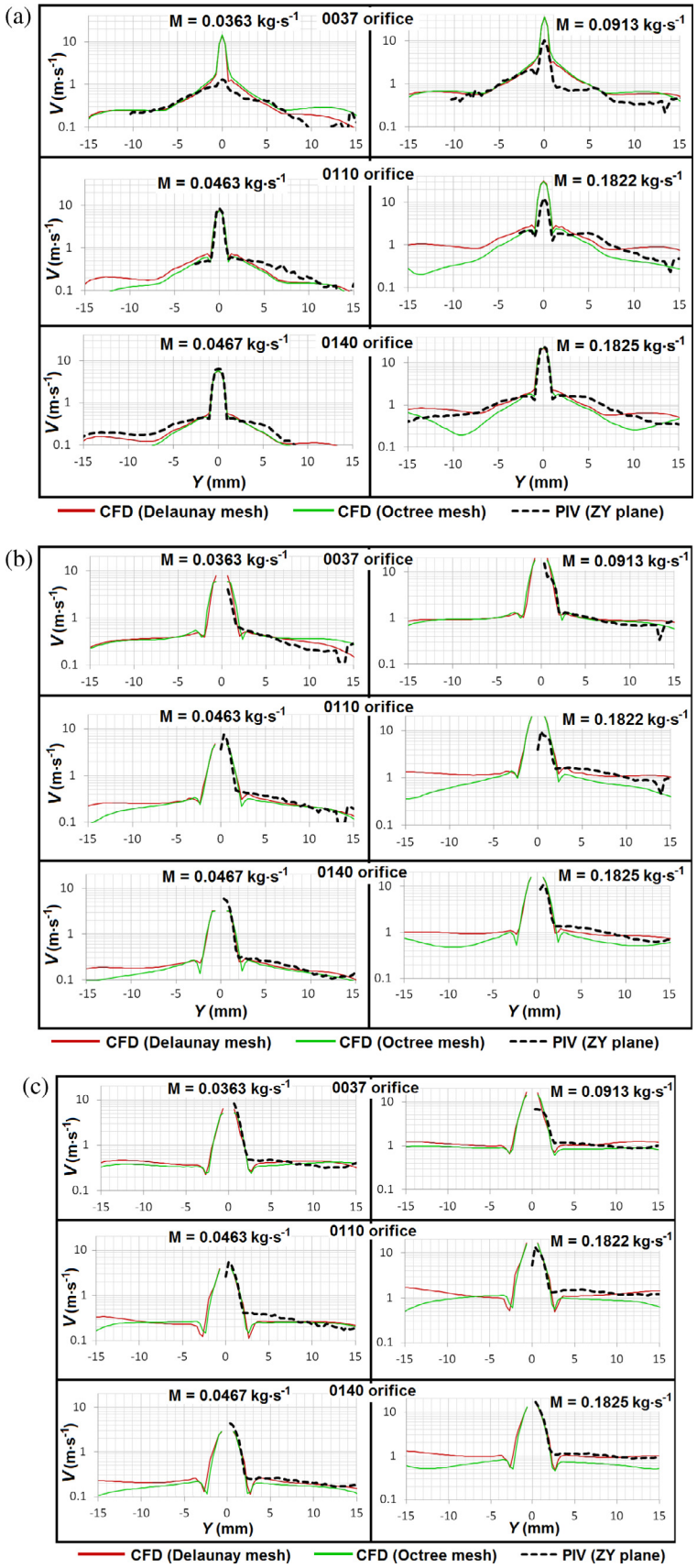

Fig. 13. Montages of graphs of velocity magnitude in ZY plane along lines at (a) $z = 1$ mm; (b) $z = 5$ mm; (c) $z = 10$ mm.

present research, following as this does in the footsteps of the techniques used previously. Nonetheless, there is as much scientific merit in presenting the limitations of techniques, as of obtaining successful results via those techniques. Hence the turbulence fields are compared below using the same line-graph techniques as for velocity magnitude, doing so in the hope that any limitations in the current techniques can be understood better, and future research aided in identifying improvements in validation techniques.

The two turbulent fields considered were turbulent kinetic energy (k) and turbulent energy dissipation (ε). The latter is particularly important in terms of its impact upon chemical reactions (micromixing) and in emulsification (maximum drop size). In CFD these were directly outputted from the SST-SAS turbulence model, and results are given below for both Delaunay and Octree meshes to help demonstrate mesh independence. In PIV the turbulent variables had to be derived from the 2D velocity statistics at each point using an isotropic assumption. The equations are given above in the methods section; equations (1), (2) and (3) for k, ε_{de} and ε_{sgs} respectively, which have been adapted from the derivations of Gabriele et al. (2009). Two version of ε are used since the DE method tends to underestimate due to the finite grid scale; the SGS method attempts to add back in the missing effect of the smallest turbulent eddies.

In summary: turbulent kinetic energy (k) was compared between two CFD meshes and the PIV results; turbulent dissipation rate (ε) was compared between two CFD meshes and two types of PIV estimate; both of these for the medium flow rate, medium orifice and blade out where a successful velocity comparison had been obtained. Axial comparison graphs are given first for k and ε in Fig. 14; then ZY cross-sectional comparison graphs are given for k and ε in Fig. 15.

Turbulent kinetic energy (k) was compared between CFD and PIV along the Sonolator axis (Fig. 14a) and at cross-sections in the ZY plane at four distances from the orifice (Fig. 15a). Between

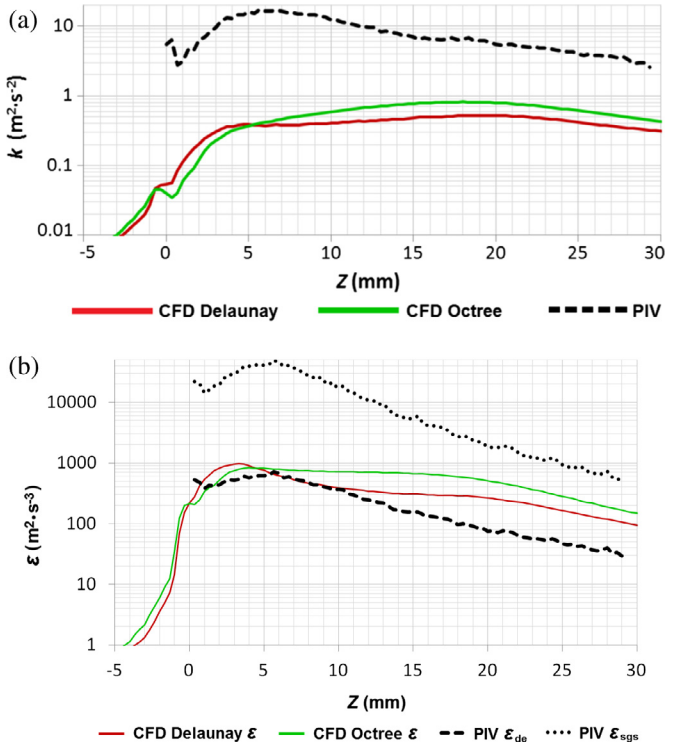

Fig. 14. Graphs along the axial line for blade-out, middle case (0110 orifice, 0.092 kg s^{-1}) of (a) turbulent kinetic energy k, (b) turbulent dissipation rate ε.

CFD and PIV the variable k broadly agreed in pattern and moved in the same direction. However, inspection of the data indicated that k from PIV was around 10–50 times the magnitude of k from CFD. One possible explanation is that the CFD k data was from transient simulations and included only high frequency turbulent components and not low frequency jet oscillations, however the PIV data was time-averaged across 500 PIV frames, and would have included both periodic jet oscillations and true turbulent variation, which increased the k measurements greater than the true turbulent value. The reason the jet oscillations could not be separated in PIV was since PIV images were taken around 7 times a second, and the jet oscillation was faster than this and not absolutely fixed in period. Hence a single jet frequency could not be isolated from PIV velocity data time series, and its effect could not be deducted from k here. Further work is needed to separate out periodic and turbulent components of the PIV data in order to get better agreement with CFD k data and also to compare jet oscillation period and magnitude between CFD and PIV.

Overall, the k output of the CFD simulations may have been reliable, since the PIV k was likely to be an overestimate due to jet oscillation, but it was not possible to confirm the degree of PIV overestimation in these sets of experiments. It should be noted that no regular patterns of vortices were observed in either PIV or CFD data, the latter can of course be interrogated beyond the temporal frequency limit of the PIV data set. This is likely due to the Reynolds number being well into the turbulent regime, and a regular pattern of vortex shedding would only be expected near the transitional regime.

Turbulent energy dissipation (ε) was also compared between CFD and PIV along the Sonolator axis (Fig. 14b) and at cross-sections in the ZY plane at four distances from the orifice (Fig. 15b). Here the general result was that the values of ε from CFD (using the SST-SAS turbulence model) were bounded below by ε_{de} from PIV, and above by ε_{sgs} from PIV. Hence the DE method provided a lower bound, and the SGS provided an upper bound. This may be explained since DE (direct evaluation) is an exact evaluation of the turbulent stresses in the fluid, but for PIV using a grid scale above the Kolmogorov length scale the smallest eddies are not measured and the turbulent dissipation therefore underestimated (Sheng et al., 1998; Gabriele et al., 2009). Conversely, for the SGS (sub-grid scale) method a model is used to estimate the turbulent stresses below the grid scale and add them back into the measurement. This model, in the absence of detailed eddy size data, cannot give accurate results in every scenario; it assumes (for the basic SGS model used here) a single eddy scale across the whole flow, whereas the Sonolator has wide variations in velocity. The SGS model contains a constant factor (the Smagorinsky constant) of 0.17; other research (Gabriele et al., 2009) showed that for a stirred tank application a constant of 0.11 gave better results. Hence the SGS model is known to overestimate in some circumstances, as appears the case in this work.

Two places where a good comparison was obtained between ε_{de} and ε from CFD were: (1) in the recirculation region a long way from the jet, and (2) on the Sonolator axis directly after the orifice, up to around z = 10 mm. The reason for the first was likely to be that the lower turbulence levels away from the jet had larger eddy sizes which were better captured by PIV and by the DE method. The reason for the second could be that turbulence was higher on the jet boundary than in the centre of the jet, hence the relatively undisturbed fast region in the jet centre also had eddies captured well by PIV and the DE method.

Overall, the comparison of ε values between CFD and PIV could not provide conclusive validation of ε from CFD, however the magnitude of ε from CFD was within bounds suggested by DE and SGS analysis on PIV data, making CFD ε believable, correlating well with ε_{de} calculated using the DE method on the PIV data.

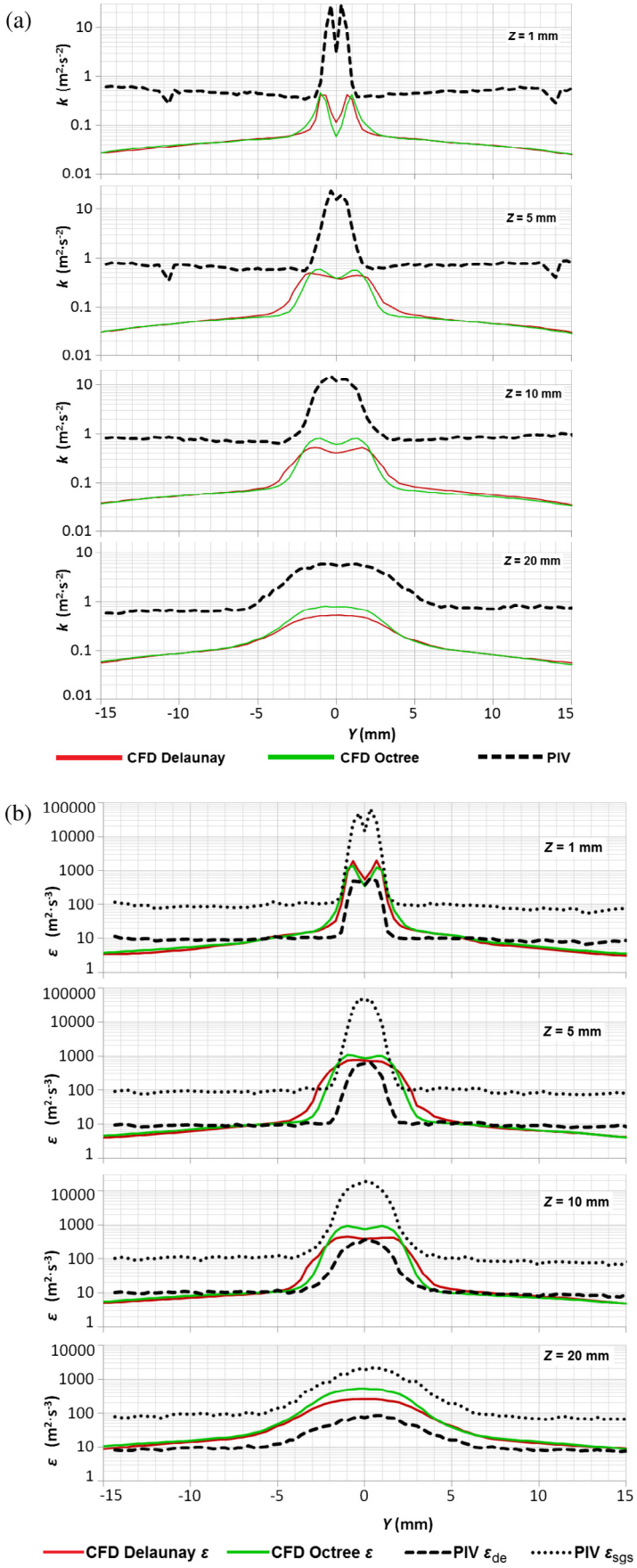

Fig. 15. Graphs along cross-sections in ZY plane for blade-out, middle case (0110 orifice, 0.092 kg s^{-1}) of (a) turbulent kinetic energy k, (b) turbulent dissipation rate ε.

4. Conclusions

PIV experiments and CFD simulations were carried out successfully for a Sonolator liquid whistle mixer. CFD simulation results for the Sonolator were compared against experimental results from PIV in order to validate the CFD simulations. Flow variables considered included: pressure drop over the Sonolator, velocity, turbulent kinetic energy (k) and turbulent energy dissipation rate (ε).

Predicted pressure drop across the Sonolator from CFD was comparable with pressure drops measured during PIV experiments. CFD velocity validation was good where PIV data was known to be accurate. From these cases, it was possible to extend validation (by using scaling rules and similarity between geometric cases) to some cases (and locations) where PIV data was found to be less accurate. Turbulent kinetic energy (k) was similar in pattern from CFD to PIV, but was lower in magnitude in CFD. The extra magnitude of the turbulent kinetic energy obtained from PIV was thought to be due to periodic components which could not be removed from those results. It was therefore possible that turbulent kinetic energy obtained from CFD was of the right magnitude.

CFD ε was bounded in most locations and cases by PIV ε_{de} and PIV ε_{sgs}, and followed their general pattern. In regions with lower turbulence (and fewer sub-grid eddies) CFD ε was of comparable magnitude to PIV ε_{de} and thus validated. In the higher turbulence regions CFD ε could not be explicitly validated, but due to being bounded by PIV ε_{de} and PIV ε_{sgs} it was of a realistic magnitude.

These findings have demonstrated that CFD can be used with reasonable confidence in predicting the behaviour of the Sonolator device; the bounds of values of energy dissipation defined are important for practitioners who are using such devices for the emulsification of liquid-liquid products, chemical reaction or mixing.

Acknowledgements

DJR was sponsored by the EPSRC Industrial Doctorate Centre in Formulation Engineering (EP/G036713/1) and Unilever Port Sunlight.

The assistance of Federico Alberini, Robert Sharpe (Bob) and Phil Harris (Bill), Andrea Gabriele and Julia Hofinger from the School of Chemical Engineering with different aspects of the work are acknowledged. We also acknowledge Rob Brakeman, Sonic Corp. (http://www.sonicmixing.com) for providing technical drawings of the Sonolator for CFD geometry and Jumpstart UK (employer) for providing DJR with CPD time for writing of his EngD thesis Ryan (2015) and this paper.

References

Chand, R., Bremner, D.H., Namkung, K.C., Collier, P.J., Gogate, P.R., 2007. Water disinfection using the novel approach of ozone and a liquid whistle reactor. Biochem. Eng. J. 35 (3), 357–364.

Clark, A., Dewhurst, R.J., Payne, P.A., Ellwood, C., 2001. Degassing a liquid stream using an ultrasonic whistle. In: Yuhas, D.E., Schneider, S.C. (Eds.), IEEE Ultrasonics Symposium Proceedings, vols. 1 and 2 of Ultrasonics Symposium, pp. 579–582.

Drumm, C., Bart, H.J., 2006. Hydrodynamics in a RDC extractor: single and two phase PIV measurements and CFD simulations. Chem. Eng. Technol. 29 (11), 1297–1302.

Egorov, Y., Menter, F., 2008. "Development and Application of SST-SAS Turbulence Model in the DESIDER Project", Advances in Hybrid RANS-LES Modelling. Springer, Berlin, Heidelberg, pp. 261–270.

Egorov, Y., Menter, F.R., Lechner, R., Cokljat, D., 2010. The scale-adaptive simulation method for unsteady turbulent flow predictions Part 2 application to complex flows. Flow Turbul. Combust. 85 (1), 139–165.

Feng, K., Benra, F.-K., Dohmen, H.K., 2009. Comparison of Periodic Flow Fields in a Radial Pump among CFD, PIV and LDV Results. Int. J. Rotating Mach. 2009, Article ID: 410838.

Ford, M.D., Nikolov, H.N., Milner, J.S., Lownie, S.P., DeMont, E.M., Kalata, W., Loth, F., Holdsworth, D.W., Steinman, D.A., 2007. PIV measured versus CFD predicted flow dynamics in anatomically realistic cerebral aneurysm models. J. Biomech. Eng. 130 (2), 021015.

Gabriele, A., Nienow, A.W., Simmons, M.J.H., 2009. Use of angle-resolved PIV to estimate local specific energy dissipation rates for up- and down-pumping pitched blade agitators in a stirred tank. Chem. Eng. Sci. 64, 126–143 (article plus later erratum).

Gabriele, A., Tsoligkas, A.N., Kings, I.N., Simmons, M.J.H., 2011. Use of PIV to measure turbulence modulation in a high throughput stirred vessel with the addition of high Stokes number particles for both up- and down-pumping configurations. Chem. Eng. Sci. 66 (5862), 5874.

Gandhi, M.S., Sathe, M.J., Joshi, J.B., Vijayan, P.K., 2011. Two phase natural convection: CFD simulations and PIV measurement. Chem. Eng. Sci. 66 (3152), 2171.

Hernández Jiménez, F., Sánchez Delgado, S., Gómez García, A., Acosta Iborra, A., 2011. Comparison between two fluid model simulations and particle image analysis & velocimetry (PIV) results for a two dimensional gas solid fluidized bed. Chem. Eng. Sci. 66 (3753), 3772.

Keane, R.D., Adrian, R.J., 1991. Optimization of particle image velocimeters: II Multiple pulsed systems. Meas. Sci. Tech. 2, 963–974.

Menter, F.R., 1993. Zonal Two Equation k-ω Turbulence Models for Aerodynamic Flows, AIAA, 24th Fluid Dynamics Conference, July 6–9, 1993, Orlando, Florida.

Menter, F.R., 1994. Two-equation eddy-viscosity turbulence models for engineering applications. AIAA J. 32 (8), 1598–1605.

Nakiboğlu, G., Gorlé, C., Horváth, I., Beeck, J., Blocken, B., 2009. Stack gas dispersion measurements with large scale PIV aspiration probes and light scattering techniques and comparison with CFD. Atmos. Environ. 43 (21), 3396–3406.

Nussbaumer, T., Kienner, M., 2013. Moving Grate Combustion Optimisation With CFD And PIV. <http://www.ieabcc.nl/workshops/task32_2013_CPH/08_nussbaumer_kiener_paper.pdf> (downloaded Aug 2008).

Ranade, V.V., Perrard, M., Le Sauze, N., Xuereb, C., Bertrand, J., 2001. Trailing vortices of Rushton turbine: PIV measurements and CFD simulations with snapshot approach. Trans. IChemE, 79.

Ryan, D., Simmons, M., Baker, M., 2011. Modelling multiphase jet flows for high velocity emulsification. In: Proceedings of ASME-JSME-KSME Joint Fluids Engineering Conference, 24–29 July 2011, Hamamatsu, Japan, Paper number AJK2011-03023.

Ryan, D., Simmons, M. and Baker, M. (2013). "Investigating Dispersion and Emulsification Processes using a Sonolator Liquid Whistle", Proceedings of 8th International Conference on Multiphase Flow, 26–31 May 2013, Jeju, Korea.

Ryan, D.J., 2015. Investigation of fluid dynamics and emulsification in sonolator liquid whistles. EngD Thesis, University of Birmingham, UK.

Sheng, J., Meng, H., Fox, R.O., 1998. Validation of CFD simulations of a stirred tank using particle image velocimetry data. Can. J. Chem. Eng. 76.

Silva, G., Leal, N., Semiao, V., 2008. Micro PIV and CFD characterization of flows in a microchannel: velocity profiles, surface roughness and Poiseuille numbers. Int. J. Heat Fluid Flow 29 (1211), 1220.

Virdung, T., Rasmuson, A., 2007. Hydrodynamic properties of a turbulent confined solid liquid jet evaluated using PIV and CFD. Chem. Eng. Sci. 62 (5963), 5978.

Westra, R.W., Broersma, L., van Andel, K., Kruyt, N. P., 2010. PIV measurements and CFD computations of secondary flow in a centrifugal pump impeller. J. Fluid Eng. (ASME) 132.